

NiCo₂O₄@quinone-rich N–C core–shell nanowires as composite electrode for electric double layer capacitor

Yanli Fang¹, Hui Wang (✉)¹, Xuyun Wang¹, Jianwei Ren², Rongfang Wang¹

¹ State Key Laboratory Base for Eco-Chemical Engineering, College of Chemical Engineering,
Qingdao University of Science and Technology, Qingdao 266042, China

² Department of Mechanical Engineering Science, University of Johannesburg, Johannesburg 2006, South Africa

© Higher Education Press 2022

Abstract The bind-free carbon cloth-supported electrodes hold the promises for high-performance electrochemical capacitors with high specific capacitance and good cyclic stability. Considering the close connection between their performance and the amount of carbon material loaded on the electrodes, in this work, NiCo₂O₄ nanowires were firstly grown on the substrate of active carbon cloth to provide the necessary surface area in the longitudinal direction. Then, the quinone-rich nitrogen-doped carbon shell structure was formed around NiCo₂O₄ nanowires, and the obtained composite was used as electrode for electric double layer capacitor. The results showed that the composite electrode displayed an area-specific capacitance of 1794 mF·cm⁻² at the current density of 1 mA·cm⁻². The assembled symmetric electric double layer capacitor achieved a high energy density of 6.55 mW·h·cm⁻³ at a power density of 180 mW·cm⁻³. The assembled symmetric capacitor exhibited a capacitance retention of 88.96% after 10000 charge/discharge cycles at the current density of 20 mA·cm⁻². These results indicated the potentials in the preparation of the carbon electrode materials with high energy density and good cycling stability.

Keywords carbon cloth, NiCo₂O₄ nanowires, core–shell structure, quinone-rich, electric double layer capacitor

1 Introduction

There is a continuous demand to shift the current fossil fuel-based energy system with the environmental issues to the environment-friendly electrochemical energy storage system. Compared to Li-ion batteries,

supercapacitors present advantages of fast charge/discharge speed and high power density. As one type of the supercapacitors, the working principle of electric double layer capacitor (EDLCs) is to generate a potential for energy storage by using electrostatic adsorption to continuously adsorb the charged ions in the electrolyte onto the electrode surface. Therefore, the electrode material as a current collector is the key component of EDLCs [1].

Very often, carbon-based materials such as carbon fibers [2], activate carbon [3] and carbon nanotubes [4] are chosen as the electrode materials due to their high electrical conductivity and excellent stability in strong acid or alkali solutions. Usually, a single carbon electrode material experimentally gave the low specific capacitance, and the compositing with other materials has been explored as a strategy to improve the overall capacitances [5,6]. In the past few years, the nanotechnology has contributed significantly to the development of EDLCs by being able to provide large specific surface area between the electrode and electrolyte, and shorten the propagation path of the electrolyte ions [7]. Taking the nanoscale effect into consideration, the construction of hybrid nanomaterials offers the potentials towards the enhanced charge/discharge capabilities [8]. Despite of the progress made so far, the studied nanohybrid materials generally exhibited the disorder structures, ease of aggregation, and eventually the low surface areas with decreased specific capacitances. In addition, the over-loading of active substances on a certain substrate will increase the thickness of the hybrid nanomaterials. Sequentially, a percentage of the active substance will be masked and unable to function properly, so as that the overall catalytic efficiency was reduced [9]. Therefore, it is particularly important to increase the loading surface area for the active substance through the preparation of the ordered or hierarchical nanoarray structure.

Clearly, the compositing of different carbon materials

will collect their respective properties and expand the structural diversity of the carbon-based materials. The preparation of the ordered nanoarrays towards the higher surface area and utilization of the active substances have been demonstrated by Ren et al. [10] and Wu et al. [11]. Particularly, the core-shell materials with a hierarchical structure have been intensively researched with different shapes of cubic, octahedron, linear, tubes and rods [12]. For instance, a hybrid core-shell carbonaceous material was prepared by Ariyanto et al. [13] with a microporous carbon core surrounded by a mesoporous graphite shell; Qian et al. [14] prepared the multi-walled carbon nanotube@mesoporous carbon composites with a core-shell configuration. Considering the correlation of surface area and specific capacitance, the construction of a core-shell structure may be a way to enhance the capacitance and increase the surface area through further activation. In contrast, the heteroatoms of N, O, S, or P-doping into carbon nanomaterials would enhance the power density of the composites by introducing additional pseudocapacitance to the capacitor [15,16]. Yamauchi and co-workers [17] firstly prepared nitrogen-doped carbon@graphitic carbon (NC@GC) nanocomposite with core-shell structure by heat treatment and seed-mediated growth methods. The composite combined the high specific surface area and nitrogen content of NC as well as the high degree of graphitization of GC. As a result, the core-shell material exhibited an enhanced electrochemical performance compared with the single carbon materials. From this point of view, the core-shell nanoarchitectures is a good concept to enhance the electrochemical performance of the electrode and artificially bring in the additional pseudocapacitance to further improve the specific capacitance [17,18].

Thus far, the lateral area for sufficient loading of active carbon substances appeared to be limited, though some efforts had been made through thermal treatment, acid etching, air calcination, as well as surface modification by oxygen-containing groups [19–21]. Those measures intended to increase the loading capacity through roughening the surface of the substrate and creating structural defects. Alternatively, Liao et al. [22] fabricated the nickel nanowire arrays @Co(OH)₂ composite electrode via a hydrothermal approach by homogeneously depositing Co(OH)₂ nanoflakes on nickel nanowire arrays. The as-prepared one-dimensional system displayed a lavender-like structure with a high specific surface area of 74.5 m²·g⁻¹. Pan et al. [23] fabricated a vertically aligned hierarchical array structure by using the accordion-structured MXene particles as the building block. The micro-scale composite material was claimed to prevent the restacking of the two-dimensional nanomaterials and facilitate the ion migration as well as electron transport in the all-solid-state supercapacitors. As summarized in Table 1, the hierarchical array structure was concluded as a solution to increase the specific surface area and the

utilization rate by alleviating the restacking of active substances.

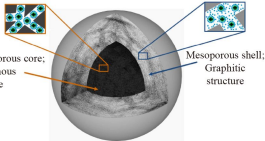
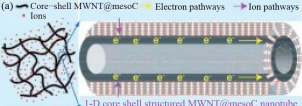

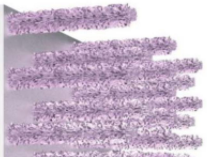
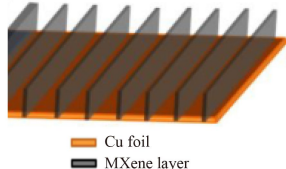
Given the excellent conductivity and porous structure of NiCo₂O₄ nanowires [24], in this study, NiCo₂O₄ nanowires were chosen to grow on the carbon substrate, so as that the low conductivity can be compensated while using the nanowires as a support to increase the available longitudinal surface area for the further deposition of carbon nanomaterials. Then, the NiCo₂O₄ nanowire-grown activated carbon cloth (MNW@ACC) was then coated with a layer of dopamine (PDA-MNW@ACC) through a polymerization reaction. Sequentially, the PDA was converted into an N-doped carbon layer by the high-temperature carbonization [20]. Up to now, an NC-shell structure was formed around the NiCo₂O₄ nanowires as a core-shell composite electrode material (NC-MNW@ACC). On the basis of N-doping, the surface area and oxygen-containing functional groups of the resultant core-shell NC-MNW@ACC composite were further increased by going through the electrochemical oxidation driven by the high-voltage in the mixed acids. Eventually, a core-shell quinone-rich QNC-MNW@ACC sample was obtained with the enhanced areal-specific capacitance and cycling stability for EDLCs.

2 Experimental

The commercial CC was sonicated into acetone, ethanol and de-ionized water under ultrasound for 20 min, respectively. The dried CC sample was placed into a tube furnace, which was heated up to 450 °C at 5 °C·min⁻¹ and kept at that temperature for 2 h to yield ACC. Then, 8 mmol of Co(NO₃)₂·6H₂O, 4 mmol of Ni(NO₃)₂·6H₂O and 12 mmol of CO(NH₂)₂ were dissolved together into a mixed solution containing 30 mL de-ionized water and 30 mL ethanol. After 30 min stirring, 2 cm × 3 cm ACC sample was immersed into the solution, and the mixture was transferred into a Teflon-lined reactor. After another 6 h reaction at 150 °C, the sample was rinsed and dried at 60 °C in an oven to obtain the MNW@ACC. Sequentially, the MNW@ACC sample was immersed into HCl-Tris (pH = 8.5), and the mixture was stirred for 24 h after adding a certain amount of DA solution (1 mg·mL⁻¹). After rinsing with de-ionized water and dried in the oven, the PDA-MNW@ACC sample was obtained, which was placed in a tube furnace and heat-treated at 700 °C under N₂ atmosphere for 2 h to yield NC-MNW@ACC. Lastly, NC-MNW@ACC sample was immersed into the concentrated HNO₃/H₂SO₄ acid mixture and 3 V voltage was applied for 8 min to yield QNC-MNW@ACC.

For comparison, ACC samples loaded with QNC-ACC without growing NiCo₂O₄ nanowires was also prepared by following the same procedure.

Table 1 Different hierarchical core-shell structures

Structure	Preparation	Advantage	Electrochemical performance	Ref.
 <p>Microporous core; Amorphous structure</p> <p>Mesoporous shell; Graphitic structure</p>	<ul style="list-style-type: none"> Extraction Chlorination 	Homogeneous pore structures; good capacitance retention	Power densities more than $40 \text{ kW} \cdot \text{kg}^{-1}$ at energy densities reaching $27 \text{ kW} \cdot \text{kg}^{-1}$ [13]	
 <p>(a) Core-shell MWNT@mesoC</p> <p>Electron pathways</p> <p>Ion pathways</p> <p>1-D core-shell structured MWNT@mesoC nanotube</p>	<ul style="list-style-type: none"> Sol-gel methods Nano casting 	Highly conductive multiwall carbon nanotube core and mesoC shell with short-pore-length	Specific capacitance of $60.2 \text{ F} \cdot \text{g}^{-1}$ at the current density of $5 \text{ mV} \cdot \text{s}^{-1}$ [14]	
 <p>Nitrogen-doped carbon @graphitic carbon</p>	<ul style="list-style-type: none"> Seed-mediated growth method Thermal treatment 	Large surface area of nitrogen-doped carbon and high graphitic level of graphitic carbon	Specific capacitance of $270 \text{ F} \cdot \text{g}^{-1}$ at the current density of $2 \text{ A} \cdot \text{g}^{-1}$ [17]	
	Hydrothermal	High surface area and high quality load	High specific capacitance of $891.2 \text{ F} \cdot \text{g}^{-1}$ at the current density of $1 \text{ A} \cdot \text{g}^{-1}$ [22]	
 <p>Cu foil</p> <p>MXene layer</p>	<ul style="list-style-type: none"> Spray Hot pressing 	Retain the accordion structure of MXene and possess a micron-scale array structure	Volumetric capacity of $485 \text{ F} \cdot \text{cm}^{-3}$ under the current density of $0.5 \text{ A} \cdot \text{cm}^{-3}$ [23]	

3 Results and discussion

Figure 1 illustrates the schematic procedure of QNC-MNW@ACC sample and the detailed preparation steps can be found in the Experimental. Figure 2 shows the scanning electron microscope (SEM) images of the ACC, MNW@ACC, NC-MNW@ACC and QNC-MNW@ACC samples at different magnifications. As observed from SEM images in Figs. 2(a-1-a-3), the surface of substrate still remains relatively smooth after the air calcination process. The growth of NiCo_2O_4 nanowires under solvothermal reaction are reflected by the changes of the glossiness in the SEM images of MNW@ACC sample in Figs. 2(b-1-b-2). With the closer look of the SEM images in Figs. 2(b-3-b-5), the reed-like NiCo_2O_4 nanowires can be clearly seen to be interconnected. Meanwhile, the glossiness reduction is noticeable from the SEM images of NC-MNW@ACC sample in Figs. 2(c-1-c-3), which suggests the formation of the NC shell structure around NiCo_2O_4 nanowires. After the further electrochemical oxidation process applied in the mixed acids at 3 V for optimal 8 min, the surface of the resultant QNC-MNW@ACC sample in Figs. 2(d-1-d-3) is etched to a

certain extent and appears to be rough while NiCo_2O_4 nanowires are still under the shell-protection.

Figure 3 shows the Raman spectra and I_D/I_G values of ACC, MNW@ACC, NC-MNW@ACC and QNC-MNW@ACC four samples. As seen from Fig. 3(a), the D and G bands appear at 1320 and 1600 cm^{-1} , respectively. Generally, the D band reflects the disorder or defects of the graphitic material, while G band speaks to the stretching vibration of sp^2 C atoms. The integral ratio of I_D/I_G can be used to predict the level of disorder and degree of graphitization. The higher I_D/I_G value usually implies a higher disorder in the material [25–27]. With this mind, the I_D/I_G values for ACC, NC-MNW@ACC, QNC-MNW@ACC and QNC-ACC samples are 0.99, 1.29, 1.58 and 1.28, respectively (Fig. 3(b)). Compared to the ACC sample, the N-doping into the carbon lattice will increase the intensity of D band within NC-MNW@ACC sample by introducing certain disorders and defects such as vacancies. The highest I_D/I_G value of QNC-MNW@ACC sample suggests the presence of the highest disorders and structural defects, which will sequentially provide an enabling-prerequisite with more active sites towards a faster electrochemical process. That is, the growth of NiCo_2O_4 nanowires and electrochemical

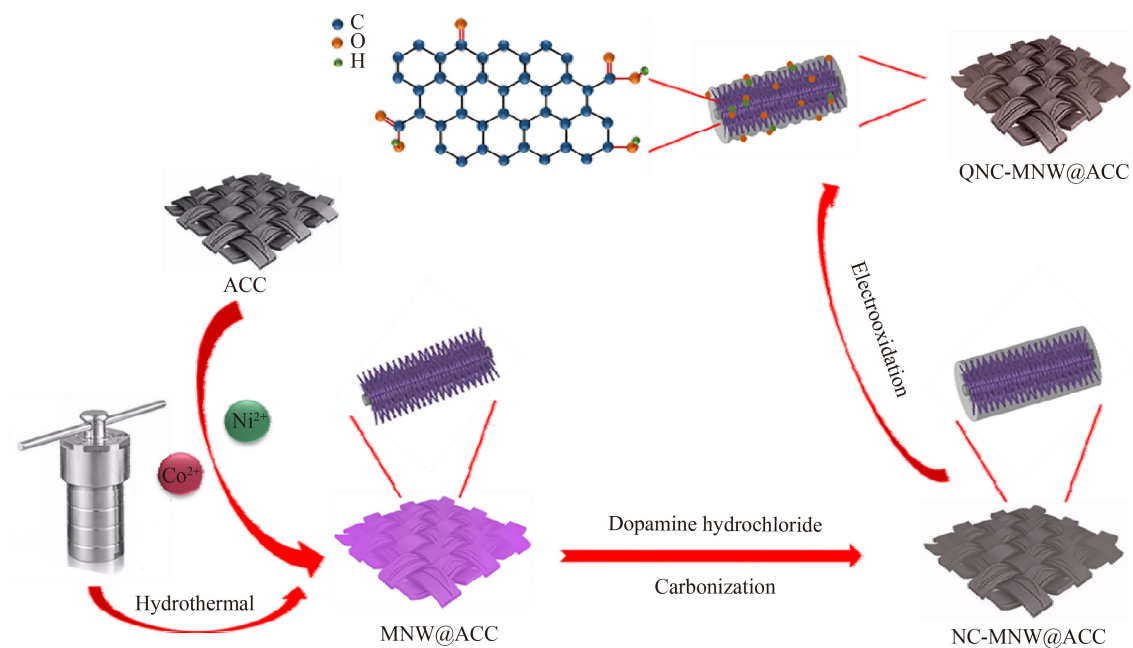


Fig. 1 Preparation procedure of QNC-MNW@ACC sample.

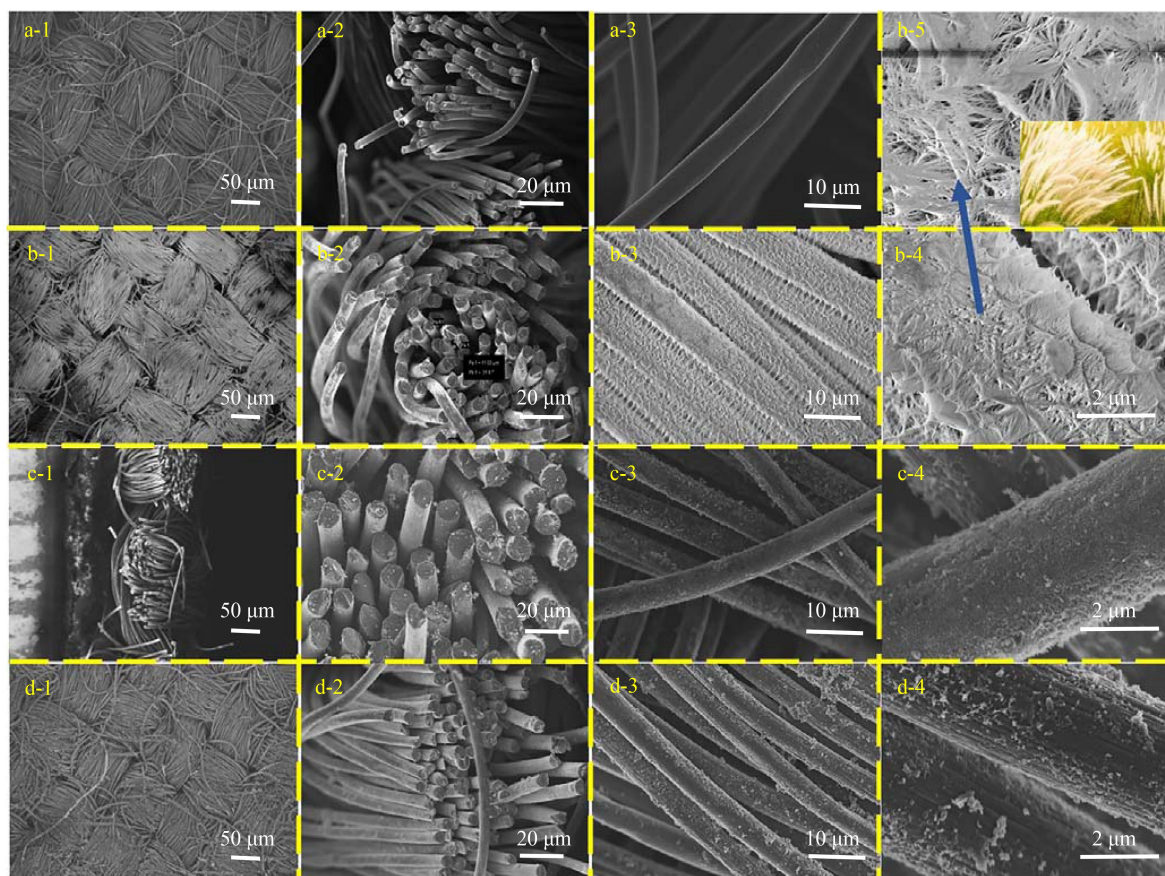


Fig. 2 SEM images of: (a-1–a-3) ACC, (b-1–b-5) MNW@ACC, (c-1–c-4) NC-MNW@ACC and (d-1–d-4) QNC-MNW@ACC samples.

oxidation treatment has effectively created the structural defects as expected. As evidenced in Fig. 3(c), in addition to the fitted peaks of 1320 cm^{-1} (D band) and 1600 cm^{-1} (G band), the peak positioned at 1500 cm^{-1} is assigned to

the sp^2 C atoms. While after the electrochemical oxidation process, two new peaks at 1220 and 1620 cm^{-1} reflect the presence of graphitization defects and the potential C=O functional groups [28].

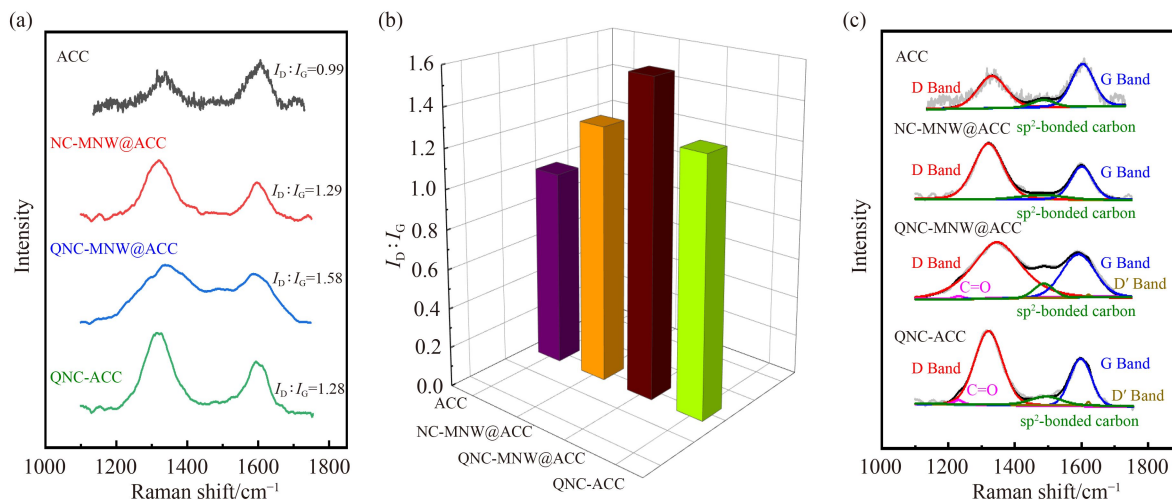


Fig. 3 (a) Raman patterns, (b) ID/IG values, and (c) fitted Raman patterns of ACC, MNW@ACC, NC-MNW@ACC and QNC-MNW@ACC samples.

X-ray electron spectroscopy (XPS) spectra of the four samples are recorded in Fig. 4 and Fig. 4(a) shows the presence of both C and O two elements in four samples. It is noticed in Fig. 4(b) that a trace amount of N element was also detected in the ACC sample, which may attribute to the impurities during the preparation of CC substrate. In contrast, the increased contents of N element within other three samples are resulted from the participation of the N-containing PDA, while the decreased C contents are caused by the C-consuming air calcination process and electrochemical oxidation treatment. In addition, the pie chart insert in Fig. 4(b) indicates an atomic percentage ratio of Co/Ni = 2:1, which agrees well with the stoichiometric ratio of NiCo₂O₄ compound. This suggests the successful growth of NiCo₂O₄ nanowires onto the ACC substrate. The C 1s XPS spectrum of QNC-MNW@ACC sample in Fig. 4(c) can be fitted into five peaks of C–C (284.7 eV), –C–OH (286.0 eV), –CN (287.0 eV), –C=O (288.5 eV) and –COOH (291.0 eV), respectively [29]. The corresponding oxygen-containing function groups displayed peaks of –C=O (531.5 eV), –C–OH (532.7 eV) and –COOH (533.8 eV) in the O 1s XPS spectrum (Fig. 4(e)). The contents of oxygen-containing functional groups (OCFG) within the NC-MNW@ACC, QNC-ACC and QNC-MNW@ACC three samples are listed in Table 2. As shown, the O content within the QNC-MNW@ACC sample increased remarkably compared to those from the other two samples, as exemplified by the –C–OH peak at 532.7 eV. This supports the conclusion that the electrochemical oxidation process favored the content loading of the oxygen-containing function groups. The N 1s high-resolution XPS spectra in Fig. 4(d) can be fitted into pyridinic-N (397.3 eV), graphitic-N (398.8 eV) and pyridinic-N oxide (403.2 eV) [30]. The presence of the –C=O functional groups enabled the formation of the pyridinic-N oxides. Meanwhile, the relatively stronger

electronegativity of O element caused the decrease of the electron density around N atoms, as a result, the binding energies of the pyridinic-N and graphitic-N species within QNC-MNW@ACC sample shifted positively compared to those of NC-MNW@ACC sample [31], which can be also evidenced in Fig. 4(e). The Co 2p high-resolution XPS spectra in Fig. 4(f) reveal the peaks of Co³⁺ (2p_{3/2}) at 779.6 eV, Co³⁺ (2p_{1/2}) at 794.1 eV, Co²⁺ (2p_{3/2}) at 781.7 eV and Co²⁺ (2p_{1/2}) at 796.4 eV, respectively. The two vibration peaks at 785.6 and 801.2 eV are satellite signals. Similarly, the Ni 2p high-resolution XPS spectrum of QNC-MNW@ACC sample in Fig. 4(g) displays four individual peaks of Ni³⁺ (2p_{3/2}) at 854.3 eV, Ni³⁺ (2p_{1/2}) at 871.8 eV, Ni²⁺ (2p_{3/2}) at (856.0 eV) and Ni²⁺ (2p_{1/2}) at 873.7 eV [24]. Referring back to the elemental contents in Fig. 4(b), NiCo₂O₄ nanowires appear to be stable in the composite before and after the electrochemical oxidation process.

To alleviate the noise effect resulting from the possible contamination and surface oxidation, the Ar-etching XPS spectra of the NC-MNW@ACC and QNC-MNW@ACC samples were also recorded in Fig. 5. As illustrated in Fig. 5(a), the content ratio of Co/Ni is close to 2:1, and the oxygen content within the QNC-MNW@ACC increased compared to that of the NC-MNW@ACC sample. This observation agrees well with Fig. 4(b) that the high-potential electrochemical oxidation loaded more oxygen-containing function groups onto the sample surface. The comparison of Fig. 5(b) and Table 2 indicates the larger content of the –C–OH functional group within the QNC-MNW@ACC sample, and such increasement contributes to the reverse pseudocapacitance through the redox reaction [32]. In comparison with Figs. 4(c–g), the C 1s, N 1s, Co 2p and Ni 2p high-resolution XPS spectra in Figs. 5(c–f) suggest that noise effect is nearly eliminated by Ar-etching technique.

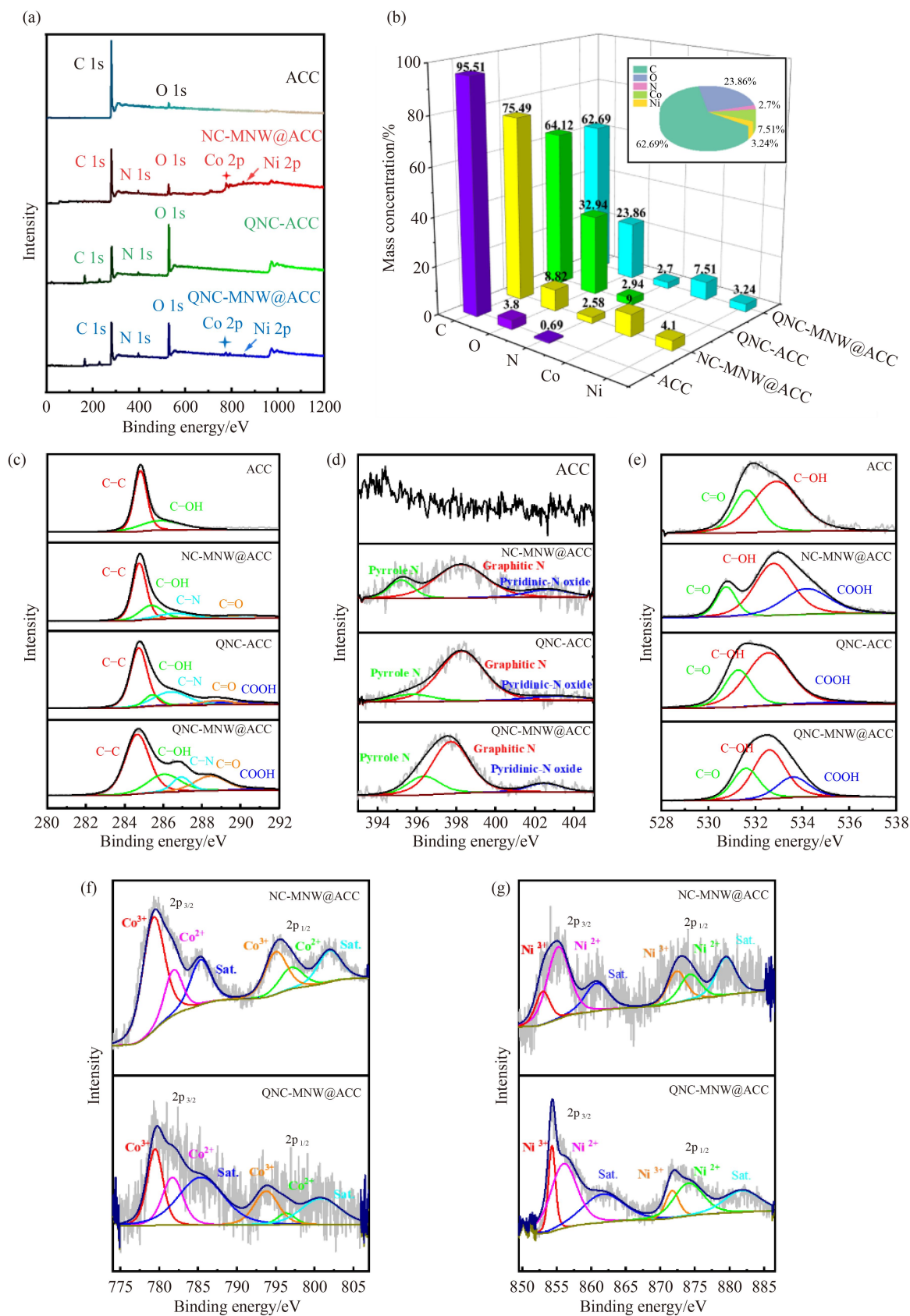


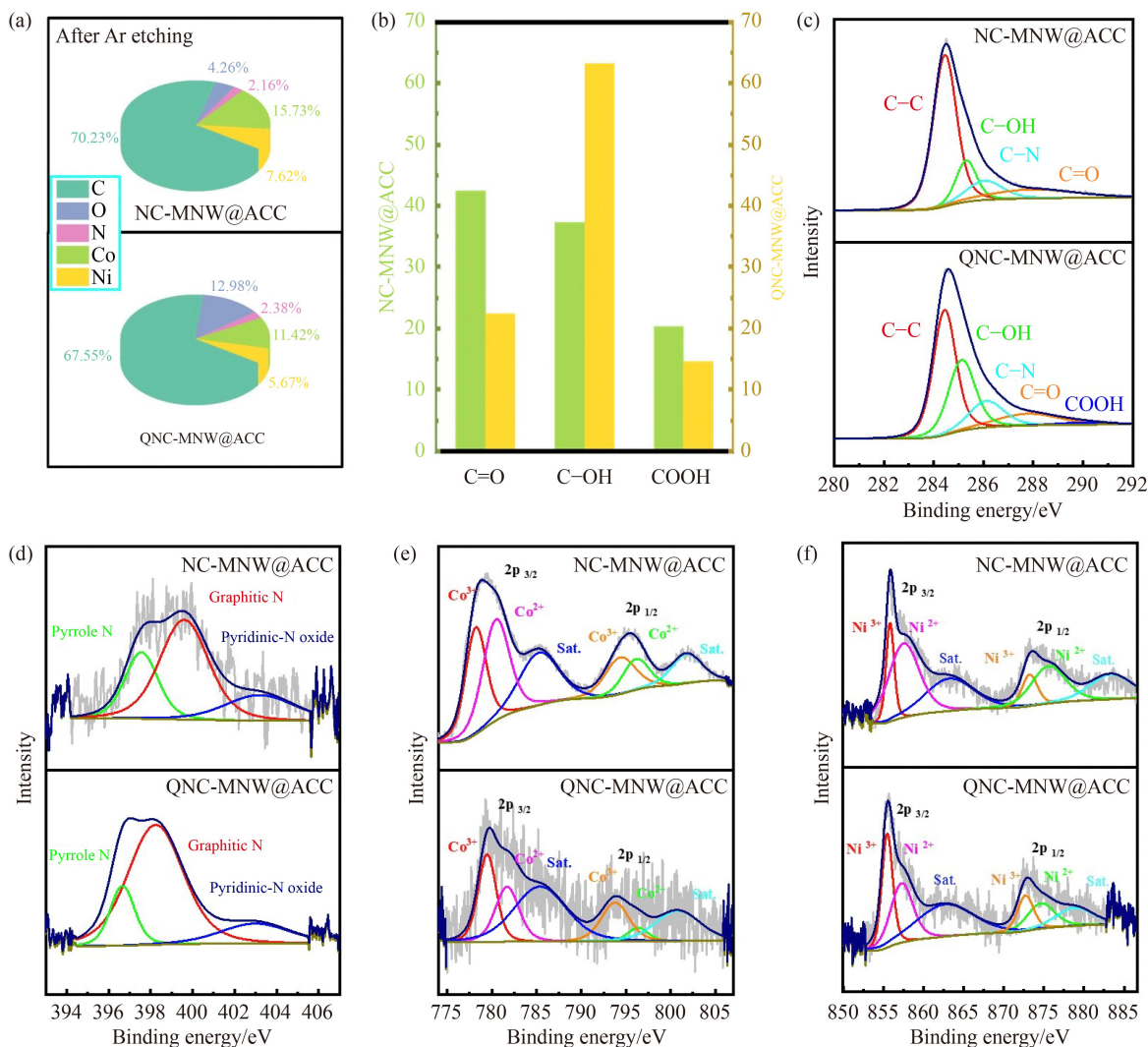
Fig. 4 XPS spectra of four samples: (a) survey spectrum, (b) elemental contents, (c) C 1s, (d) N 1s, (e) O 1s, (f) Co 2p and (g) Ni 2p.

As known, the conductivity of the electrode material plays an important role in the process of electron transfer.

During the N-doping process, the N-atoms readily entered into donor–acceptor interactions by acting as electron

Table 2 The content of OCFG in NC-MNW@ACC, QNC-ACC and QNC-MNW@ACC based on the fitted peak areas of O 1s XPS Sample

OCFG	NC-MNW@ACC	QNC-ACC	QNC-MNW@ACC
–C–OH	3945.54 (52.54%)	14232.3 (66.68%)	15771.99 (55.14%)
C=O	1196.02 (15.93%)	6235.34 (29.21%)	6821.88 (23.85%)
–COOH	2367.51 (31.53%)	876.12 (4.1%)	6009.21 (21.01%)

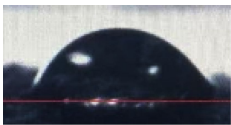

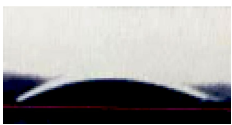
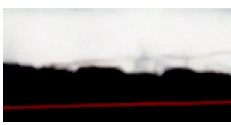
**Fig. 5** Ar-etching XPS spectra of the NC-MNW@ACC and QNC-MNW@ACC samples: (a) elemental contents, (b) the content of OCFG, (c) C 1s, (d) N 1s, (e) Co 2p and (f) Ni 2p.

donors. As evidenced by the increased I_D/I_G value in Fig. 3(b), the doping of N-atoms created the structural defects within the sample, and the N2p electrons will cross Fermi level of carbon material to occupy a higher energy level. Given the close relationship among the structural defect concentration, conductivity and Fermi surface density, the density of conduction electrons within the composite material can be improved by increasing Fermi surface density. As a result, the formation of the NC shell structure around NiCo_2O_4 nanowires increased the conductivity of the electrode material (Table 3). However, the electrochemical oxidation process was not in the favor of the conductivity. Specifically, the

substitution of O-atoms destroyed the sp^2 -hybridized carbon network, and the resultant graphitic layer with edge functional groups such as carboxyl or carbonyl groups affected the electron transfer rate negatively within the composite electrode material. Meanwhile, the substitution of N- and O-atoms significantly increased the hydrophilicity of the composite material, and the contact angle of QNC-MNW@ACC sample after carbonization and oxidation appears to be 0° .

In addition, the effects of dopamine concentration (0.5, 1, 2 $\text{mg}\cdot\text{mL}^{-1}$) and electrooxidation time (6, 8, 10 min) on the electrochemical performance were experimentally investigated. Figure 6 records the cyclic voltammetry

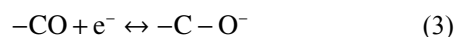
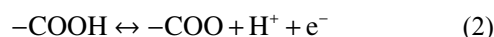
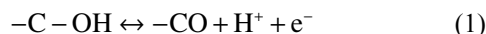
Table 3 The conductivity and contact angle of the prepared sample

Sample	ACC	PDA/ MNW@ACC	NC-MNW@ACC	QNC-MNW@ACC
Conductivity/(S·mm ⁻¹)	2.958	0.459	3.465	3.018
Contact angle				

(CV) curves at 5 mV·s⁻¹ and galvanostatic charge/discharge (GCD) curves at 1 mA·cm⁻², respectively. As shown, the electrochemical performance at 1 mg·mL⁻¹ is better than that at 0.5 mg·mL⁻¹. This is contributed by the higher-loading of N-carbon shells from PDA, which however would destroy the NiCo₂O₄ nanowires when over-weighting. In alignment with the reported results, an optimal oxidation time is also necessary to achieve the optimal number of carbon shells and eventually the best electrochemical performance [33].

Figure 7 shows the electrochemical performance of the prepared samples. As seen in Fig. 7(a), the near-rectangular shaped CV curves of the QNC-MNW@ACC sample indicates the capacitive behaviors. The oxidation-reduction peaks appeared at 0.46 V and 0.36 V attribute to the redox transition of the O-containing functional

groups on the surface of the QNC-MNW@ACC sample. Meanwhile, the integral CV areas increase with the scanning rates, and the position of the oxidation-reduction peaks shifts accordingly. This implies that the redox transition time of the O-containing functional groups are shortened with the increasing scanning rates, which can be determined from the Eqs. (1–4) below [34]:



$$i(V) = k_1 v + k_2 v^{1/2}. \quad (4)$$

Among them, $i(V)$ is the current at a specific potential,

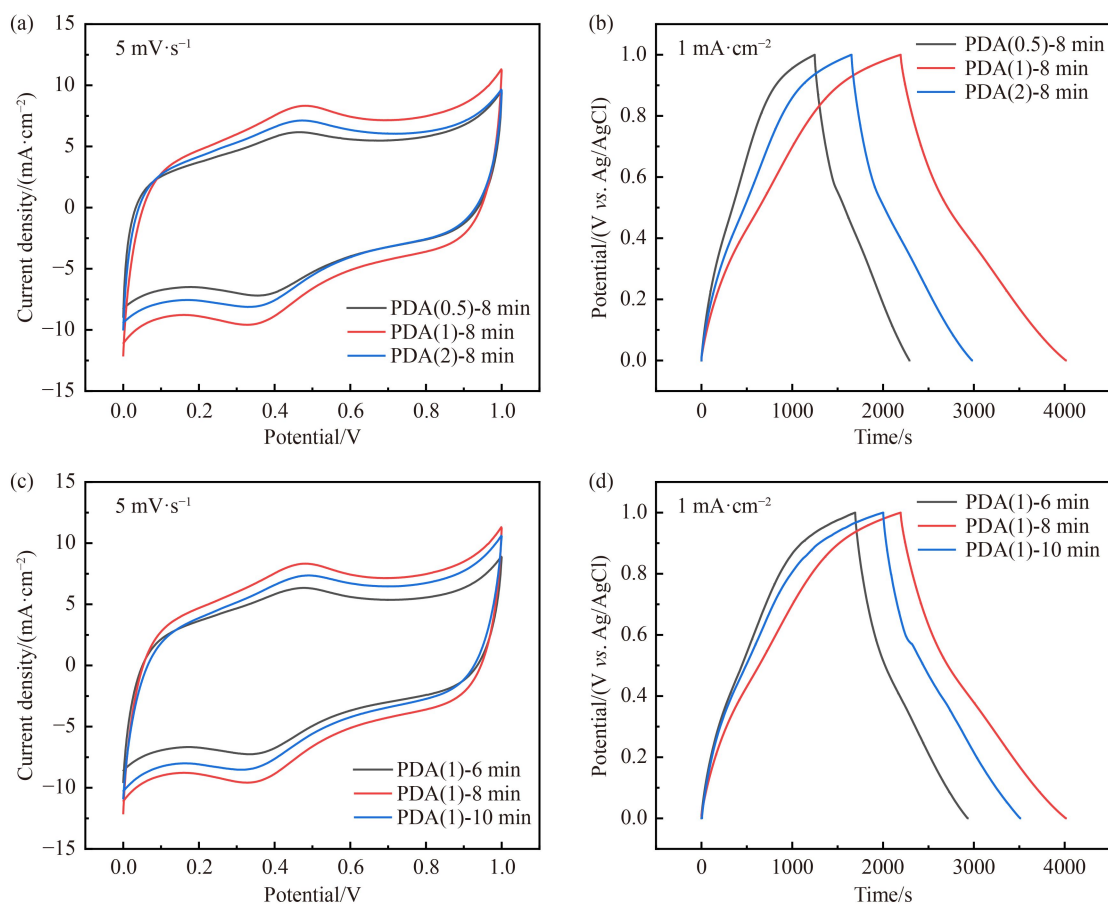


Fig. 6 (a) The CV curves at 5 mV·s⁻¹ and (b) GCD curves at 1 mA·cm⁻² for PDA(0.5)-8 min, PDA(1)-8 min, PDA(2)-8 min; (c) the CV curves at 5 mV·s⁻¹ and (d) GCD curves at 1 mA·cm⁻² for PDA(1)-6 min, PDA(1)-8 min, PDA(1)-10 min.

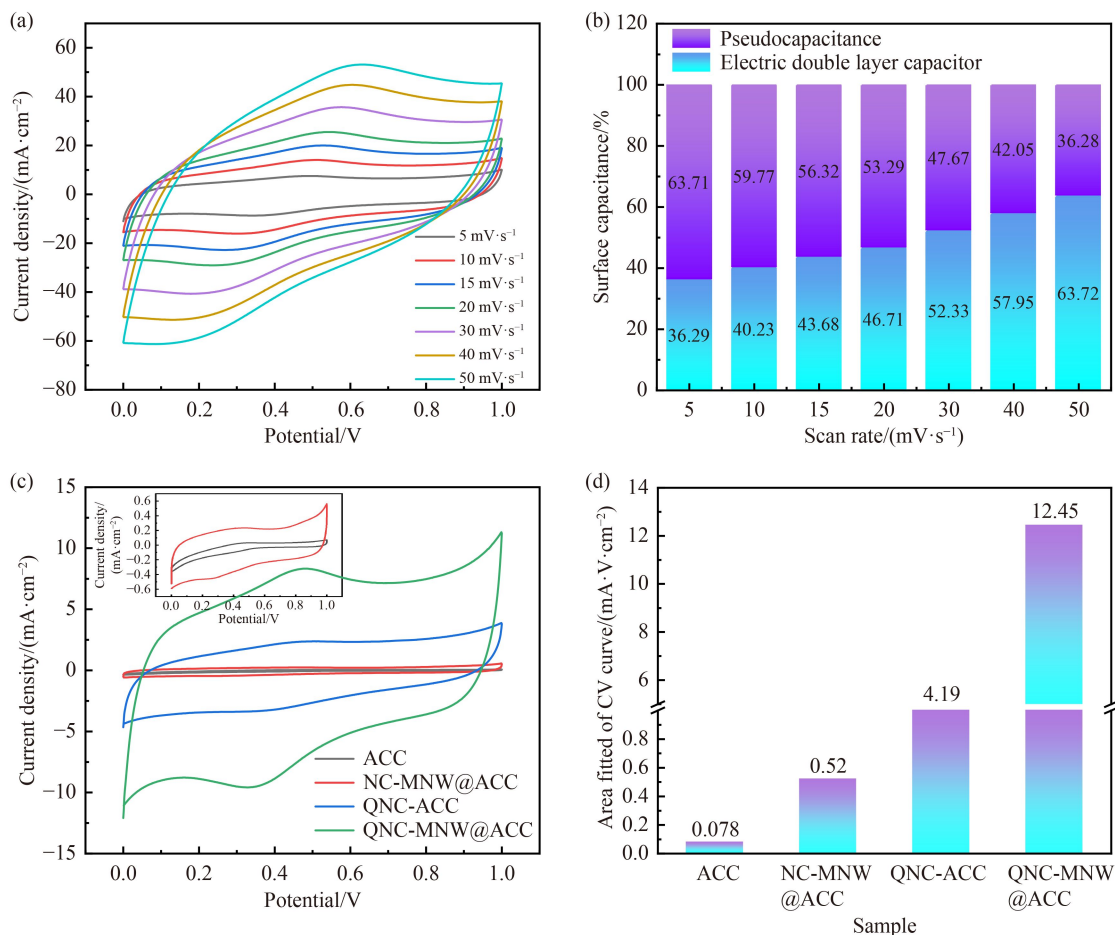


Fig. 7 (a) CV curves of QNC-MNW@ACC sample scanned at 5–50 mV·s⁻¹, (b) the capacitance contributions of EDLC and pseudocapacitance within QNC-MNW@ACC sample at different scan rates, (c) CV curves of different samples at the scan rate of 5 mV·s⁻¹, and (d) Integral areas of CV curves of different samples.

ν is the scan rate, $k_1\nu$ is the capacitive charge storage, $k_2\nu^{1/2}$ is the current controlled by the diffusion, and k_1 and k_2 are the fitting parameters. By determining k_1 and k_2 , the contribution of the diffusion-control and surface capacitance process to the current is calculated.

Based on the above equations, the capacitance contributions of EDLC within QNC-MNW@ACC sample at different scan rates were recorded [35] (Fig. 8), and the comparison is also made in Fig. 7(b). Clearly, the pseudocapacitance contribution reaches 63.71% at the scan rate of 5 mV·s⁻¹, and it drops to 36.28% when the scan rate increases to 50 mV·s⁻¹. In other words, the redox transition reactions of the O-containing functional groups within the QNC-MNW@ACC sample decreased with the increasing scan rates, which is reflected by the decreased pseudocapacitance contributions. Further, the oxidation–reduction peaks of quinone groups can be observed from the CV curves of the QNC-MNW@ACC and QNC-ACC samples in Fig. 7(c), which were scanned at a rate of 5 mV·s⁻¹. Surely, the larger integral areas of CV curves in Fig. 7(d) represent the higher current responses and electrochemical performance.

Figure 9 collects the GCD and the electrochemical impedance spectroscopy (EIS) results of the prepared samples. Figure 9(a) shows the GCD curves of the four samples at a current density of 1 mA·cm⁻², and the longest charge–discharge time suggests the largest charge–storage capacity of the QNC-MNW@ACC sample. Meanwhile, the appearance of the two plateaus in the charge/discharge curves of the QNC-MNW@ACC and QNC-ACC samples result in the poor linearity. The potentials of the plateaus are in align with those of the redox peaks in the CV curves. This indicates the presence of the quinone groups accompanied by the redox processes. Figure 9(b) shows the respective specific capacitance curve of the prepared samples at different current densities. As seen, the areal specific capacitances of QNC-ACC and QNC-MNW@ACC samples are 461.8 and 1794 mF·cm⁻² at 1 mA·cm⁻², respectively. Clearly, the growth of NiCo₂O₄ nanowires increased the charge–storage capacity of the electrode samples. The larger capacitance of the QNC-MNW@ACC sample compared to that of the NC-MNW@ACC sample (51.7 mF·cm⁻²) also suggests the positive contribution from the O-

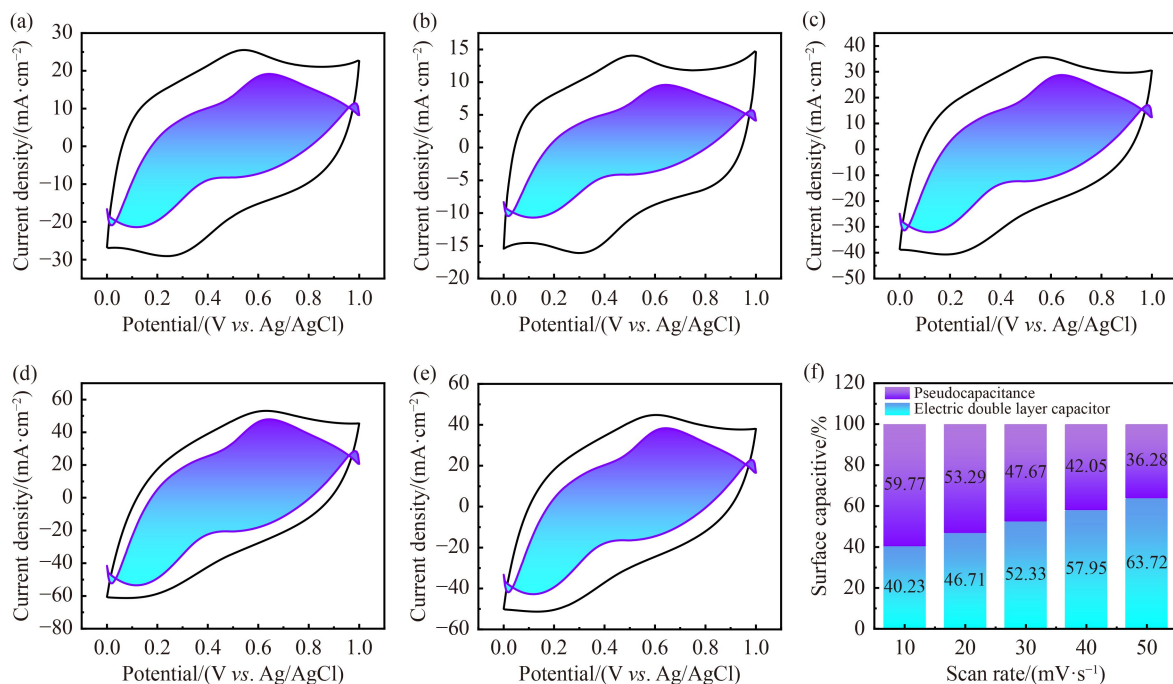


Fig. 8 (a–f) Fitting graph of double-layer capacitance contribution of QNC-MNW@ACC at scan rates of 10, 20, 30, 40, and 50 mV·s⁻¹.

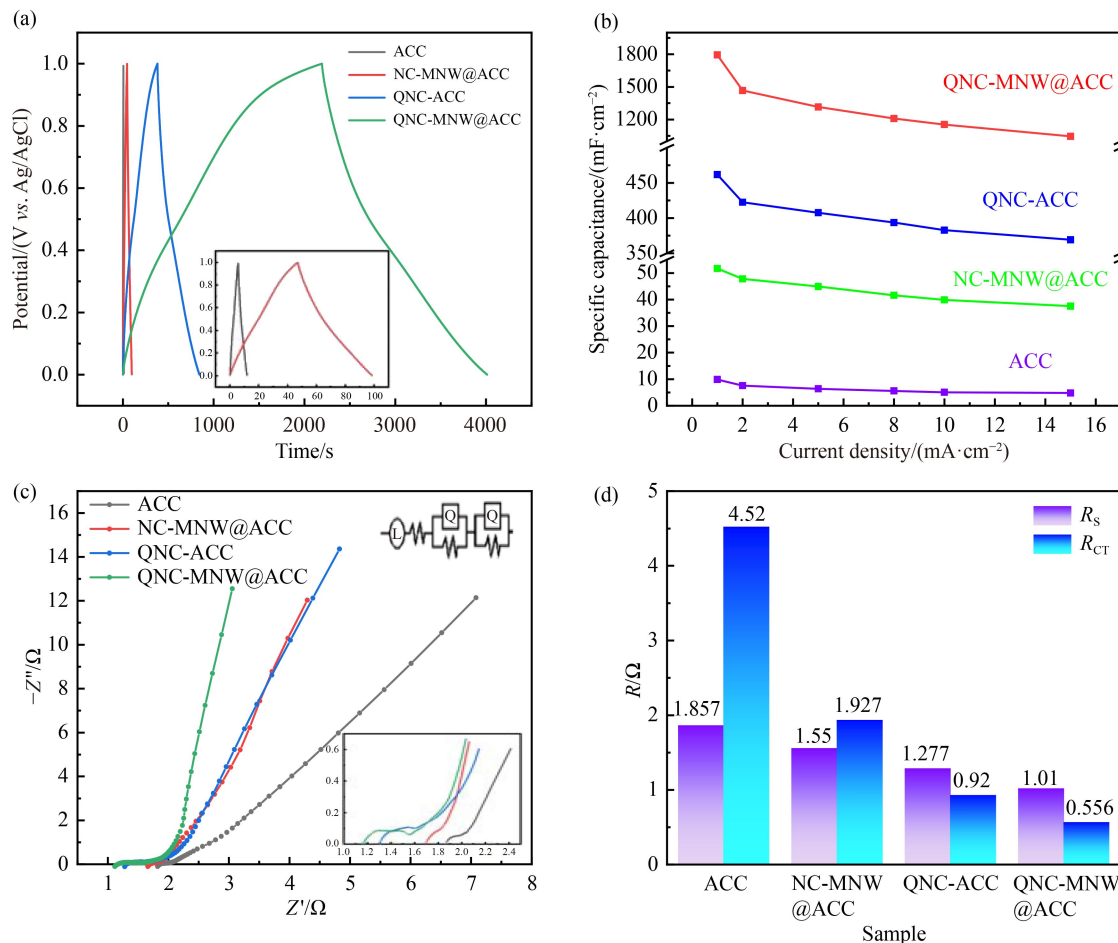


Fig. 9 (a) GCD curves at current density of 1 mA·cm⁻², (b) Areal specific capacitance at different current densities, (c) EIS of the assembled symmetric capacitors, and (d) R_s and R_{CT} values of the four ACC, NC-MNW@ACC, QNC-ACC and QNC-MNW@ACC samples.

containing functional groups. Meanwhile, the capacitance of the QNC-MNW@ACC sample retains 64.3% of the initial value when the current density increases from 1 to 15 $\text{mA}\cdot\text{cm}^{-2}$. By now, it allows us to conclude that the NC shell structure protected the core NiCo_2O_4 nanowires from contacting with electrolyte solution directly, and thus improved the structural stability of the electrode material. Meanwhile, the carbon layers with high porosity and core NiCo_2O_4 nanowires with high pore volume provided the large active surface area for the electron

transfer. With those benefits, the QNC-MNW@ACC sample displayed the smallest solution resistance ($R_s = 1.01\ \Omega$) and the lowest charge transfer resistance ($R_{CT} = 0.556\ \Omega$) in Fig. 9(c) and Fig. 9(d), respectively [36–39].

With those results in hand, the performance of the QNC-MNW@ACC-assembled symmetric capacitor is evaluated (Fig. 10). Figure 10(a) shows the CV curves measured at different operating voltages at $100\ \text{mV}\cdot\text{s}^{-1}$. As seen, the area enclosed by the CV curves with good rectangle shapes continues to increase with the applied

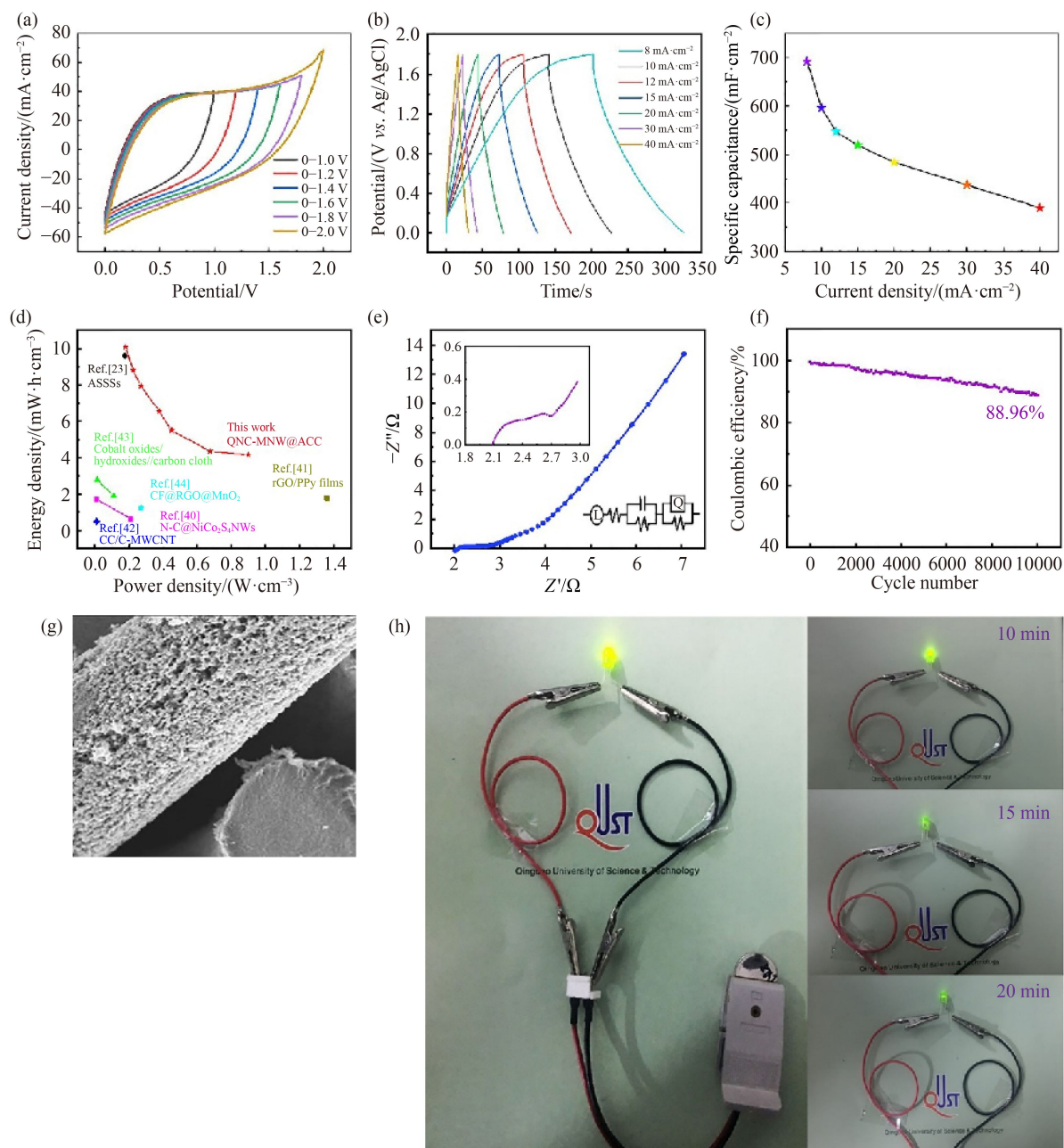


Fig. 10 Performance evaluation of the QNC-MNW@ACC-assembled symmetrical capacitor: (a) CV curves measured at different operating voltages at $100\ \text{mV}\cdot\text{s}^{-1}$, (b) GCD curves recorded over different current densities, (c) capacities vs. current densities, (d) Ragone plots of the QNC-MNW@ACC sample in comparison with the recently reported systems, (e) EIS curves, (f) long-term stability at $15\ \text{mA}\cdot\text{cm}^{-2}$, (g) SEM image of the QNC-MNW@ACC sample after long-term test, and (h) the assembled QNC-MNW@ACC-battery cell is able to power a 2.0 V LED light for over 20 min.

voltage until 1.8 V. The polarization phenomenon starts at the working voltage of 2 V. Therefore, the GCD curves are recorded over different current densities at the operating voltage window of 1.8 V. Similar to the single electrode, the GCD curves of symmetric capacitors in Fig. 10(b) present the nearly-symmetrical-triangle shapes. The capacitance decreases from 692 to 390 $\text{mF}\cdot\text{cm}^{-2}$ when the current density increases from 8 to 40 $\text{mA}\cdot\text{cm}^{-2}$, as illustrated in Fig. 10(c). The 56.4% retention rate of the initial capacitance suggests that the EDLC has good rate performance. The QNC-MNW@ACC-assembled EDLCs showed a volume energy density of 6.55 $\text{mW}\cdot\text{h}\cdot\text{cm}^{-3}$ at a power density of 180 $\text{mW}\cdot\text{cm}^{-3}$, and the energy density remained at 3.75 $\text{mW}\cdot\text{h}\cdot\text{cm}^{-3}$ when the power density increased to 900 $\text{mW}\cdot\text{cm}^{-3}$. Compared with the previously reported carbon-based electrodes (Fig. 10(d)) [23,40–44], the QNC-MNW@ACC-assembled EDLC exhibits an enhanced performance in terms of energy and power density. The Nyquist plot in Fig. 10(e) reveals the electrochemical performance of the QNC-MNW@ACC-assembled symmetrical capacitor. The excellent conductivity facilitated the charge transfer with the lower resistance values of R_s (1.84 Ω) and R_{CT} (1.81 Ω). The QNC-MNW@ACC-assembled EDLC shows a good long-term stability in Fig. 10(f) with a retention rate of 88.96% after 10000 GCD cycles at 15 $\text{mA}\cdot\text{cm}^{-2}$, and the SEM image in Fig. 10(g) displays the well-remained surface morphology of the QNC-MNW@ACC electrode after 10000 GCD cycles. Lastly, a QNC-MNW@ACC-battery cell was assembled to power a 2.0 V LED light for over 20 min (Fig. 10(h)).

4 Conclusions

In this work, a quinone-rich NC-MNW@ACC electrode material was prepared with the enhanced area-specific capacitance and pseudocapitance. Specifically, the NiCo_2O_4 nanowires were grown directly on the ACC substrate to provide the necessary surface area in the longitudinal direction, and then quinone-rich N–C shell structure was formed around NiCo_2O_4 nanowires. The optimal electrode material showed an area-specific capacitance of 1794 $\text{mF}\cdot\text{cm}^{-2}$ at a current density of 1 $\text{mA}\cdot\text{cm}^{-2}$, and a retention rate of 88.96% was displayed by the assembled symmetric capacitor after 10000 GCD cycles at 20 $\text{mA}\cdot\text{cm}^{-2}$. Besides, the NC-MNW@ACC-assembled EDLC achieved a high energy density of 6.55 $\text{mW}\cdot\text{h}\cdot\text{cm}^{-3}$ at a power density of 180 $\text{mW}\cdot\text{cm}^{-3}$. This work demonstrated a strategic way to design electrodes for electrochemical energy storage and new generation devices.

Acknowledgements The authors would like to thank the Natural Science Foundation of Shandong Province of China (Grant No. ZR2020MB024) for financially supporting this work.

References

1. Yang I, Kwon D, Kim M S, Jung J C. A comparative study of activated carbon aerogel and commercial activated carbons as electrode materials for organic electric double-layer capacitors. *Carbon*, 2018, 132: 503–511
2. Chen X, Qiu L, Ren J, Guan G, Lin H, Zhang Z, Chen P, Wang Y, Peng H. Novel electric double-layer capacitor with a coaxial fiber structure. *Advanced Materials*, 2013, 25(44): 6436–6441
3. Sun W, Lipka S M, Swartz C, Williams D, Yang F. Hemp-derived activated carbons for supercapacitors. *Carbon*, 2016, 103: 181–192
4. Qu K, Zheng Y, Jiao Y, Zhang X, Dai S, Qiao S Z. Polydopamine-inspired, dual heteroatom-doped carbon nanotubes for highly efficient overall water splitting. *Advanced Energy Materials*, 2016, 7(9): 1602068
5. Yadav S, Devi A. Recent advancements of metal oxides/Nitrogen-doped graphene nanocomposites for supercapacitor electrode materials. *Journal of Energy Storage*, 2020, 30: 101486
6. Lokhande V C, Lokhande A C, Lokhande C D, Kim J H, Ji T. Supercapacitive composite metal oxide electrodes formed with carbon, metal oxides and conducting polymers. *Journal of Alloys and Compounds*, 2016, 682: 381–403
7. Choi H, Yoon H. Nanostructured electrode materials for electrochemical capacitor applications. *Nanomaterials*, 2015, 5(2): 906–936
8. Bavier M A, Acosta G G, Kessler T, Visintin A. Flexible symmetric and asymmetric supercapacitors based in nanocomposites of carbon cloth/polyaniline-carbon nanotubes. *Energy*, 2017, 130: 22–28
9. Yang Q, Lu Z, Li T, Sun X, Liu J. Hierarchical construction of core-shell metal oxide nanoarrays with ultrahigh areal capacitance. *Nano Energy*, 2014, 7: 170–178
10. Ren Y, Yu C, Chen Z, Xu Y. Two-dimensional polymer nanosheets for efficient energy storage and conversion. *Nano Research*, 2020, 14(6): 2023–2036
11. Wu F, Liu M, Li Y, Feng X, Zhang K, Bai Y, Wang X, Wu C. High-mass-loading electrodes for advanced secondary batteries and supercapacitors. *Electrochemical Energy Reviews*, 2021, 4(2): 382–446
12. Jiang L B, Yuan X Z, Liang J, Zhang J, Wang H, Zeng G M. Nanostructured core-shell electrode materials for electrochemical capacitors. *Journal of Power Sources*, 2016, 331: 408–425
13. Ariyanto T, Dyatkin B, Zhang G R, Kern A, Gogotsi Y, Etzold B J M. Synthesis of carbon core-shell pore structures and their performance as supercapacitors. *Microporous and Mesoporous Materials*, 2015, 218: 130–136
14. Qian X, Lv Y, Li W, Xia Y, Zhao D. Multiwall carbon nanotube@mesoporous carbon with core-shell configuration: a well-designed composite-structure toward electrochemical capacitor application. *Journal of Materials Chemistry*, 2011, 21(34): 13025–13031
15. Wu Z S, Winter A, Chen L, Sun Y, Turchanin A, Feng X, Mullen K. Three-dimensional nitrogen and boron co-doped graphene for

- high-performance all-solid-state supercapacitors. *Advanced Materials*, 2012, 24(37): 5130–5135
16. Feng X, Bai Y, Liu M, Li Y, Yang H, Wang X, Wu C. Untangling the respective effects of heteroatom-doped carbon materials in batteries, supercapacitors and the ORR to design high performance materials. *Energy & Environmental Science*, 2021, 14(4): 2036–2089
 17. Tang J, Salunkhe R R, Liu J, Torad N L, Imura M, Furukawa S, Yamauchi Y. Thermal conversion of core-shell metal-organic frameworks: a new method for selectively functionalized nanoporous hybrid carbon. *Journal of the American Chemical Society*, 2015, 137(4): 1572–1580
 18. Xie C, Yang S, Xu X, Shi J W, Niu C. Core-shell structured carbon nanotubes/N-doped carbon layer nanocomposites for supercapacitor electrodes. *Journal of Nanoparticle Research*, 2020, 22(1): 25–31
 19. Zheng Y, Zhao W, Jia D, Cui L, Liu J. Thermally-treated and acid-etched carbon fiber cloth based on pre-oxidized polyacrylonitrile as self-standing and high area-capacitance electrodes for flexible supercapacitors. *Chemical Engineering Journal*, 2019, 364: 70–78
 20. Gu Y J, Wen W, Wu J M. Simple air calcination affords commercial carbon cloth with high areal specific capacitance for symmetrical supercapacitors. *Journal of Materials Chemistry A: Materials for Energy and Sustainability*, 2018, 6(42): 21078–21086
 21. Liang Z, Xia H, Liu H, Zhang L, Zhou J, Li H, Xie W. Enhanced capacitance characteristic of microporous carbon spheres through surface modification by oxygen-containing groups. *Results in Physics*, 2019, 15: 102586–102593
 22. Liao J, Wang X, Wang Y, Su S, Nairan A, Kang F, Yang C. Lavender-like cobalt hydroxide nanoflakes deposited on nickel nanowire arrays for high-performance supercapacitors. *RSC Advances*, 2018, 8(31): 17263–17271
 23. Pan Q, Duan C, Liu H, Li M, Zhao Z, Zhao D, Duan Y, Chen Y, Wang Y. Hierarchical vertically aligned titanium carbide (MXene) array for flexible all-solid-state supercapacitor with high volumetric capacitance. *ACS Applied Energy Materials*, 2019, 2(9): 6834–6840
 24. Zhang H, Xiao D, Li Q, Ma Y, Yuan S, Xie L, Chen C, Lu C. Porous NiCo_2O_4 nanowires supported on carbon cloth for flexible asymmetric supercapacitor with high energy density. *Journal of Energy Chemistry*, 2018, 27(1): 195–202
 25. Han L, Li K, Sun J, Song Q, Wang Y. Reinforcing effects of carbon nanotube on carbon/carbon composites before and after heat treatment. *Materials Science and Engineering A*, 2018, 735: 10–18
 26. Liu D, Fu C, Zhang N, Zhou H, Kuang Y. Three-dimensional porous nitrogen doped graphene hydrogel for high energy density supercapacitors. *Electrochimica Acta*, 2016, 213: 291–297
 27. Chen Y, Ji S, Wang H, Linkov V, Wang R. Synthesis of porous nitrogen and sulfur co-doped carbon beehive in a high-melting-point molten salt medium for improved catalytic activity toward oxygen reduction reaction. *International Journal of Hydrogen Energy*, 2018, 43(10): 5124–5132
 28. Bokobza L, Bruneel J L, Couzi M. Raman spectroscopic investigation of carbon-based materials and their composites. Comparison between carbon nanotubes and carbon black. *Chemical Physics Letters*, 2013, 590: 153–159
 29. Kordek K, Jiang L, Fan K, Zhu Z, Xu L, Al-Mamun M, Dou Y, Chen S, Liu P, Yin H, Rutkowski P, Zhao H. Two-step activated carbon cloth with oxygen-rich functional groups as a high-performance additive-free air electrode for flexible zinc-air batteries. *Advanced Energy Materials*, 2018, 9(4): 1802936–1802944
 30. Xiang Y, Yang T, Tong K, Fu T, Tang Y, Liu F, Xiong Z, Si Y, Guo C. Constructing flexible and self-standing electrocatalyst for oxygen reduction reaction by *in situ* doping nitrogen atoms into carbon cloth. *Applied Surface Science*, 2020, 523: 146424–146431
 31. Shen W, Fan W. Nitrogen-containing porous carbons: synthesis and application. *Journal of Materials Chemistry A: Materials for Energy and Sustainability*, 2013, 1(4): 999–1013
 32. Wang W, Liu W, Zeng Y, Han Y, Yu M, Lu X, Tong Y. A novel exfoliation strategy to significantly boost the energy storage capability of commercial carbon cloth. *Advanced Materials*, 2015, 27(23): 3572–3578
 33. Lv X, Ji S, Lu J, Zhang L, Wang X, Wang H. Quick *in situ* generation of a quinone-enriched surface of N-doped carbon cloth electrodes for electric double-layer capacitors. *Dalton Transactions*, 2021, 50(10): 3651–3659
 34. Zhang J, Li W, Ahmed Shifa T, Sun J, Jia C, Zhao Y, Cui Y. Hierarchical porous carbon foam supported on carbon cloth as high-performance anodes for aqueous supercapacitors. *Journal of Power Sources*, 2019, 439: 227066–227072
 35. Pu X, Zhao D, Fu C, Chen Z, Cao S, Wang C, Cao Y. Understanding and calibration of charge storage mechanism in cyclic voltammetry curves. *Angewandte Chemie International Edition*, 2021, 60(39): 21310–21318
 36. Itagaki M, Suzuki S, Shitanda I, Watanabe K, Nakazawa H. Impedance analysis on electric double layer capacitor with transmission line model. *Journal of Power Sources*, 2007, 164(1): 415–424
 37. Lv X, Ji S, Linkov V, Wang X, Wang H, Wang R. Three-dimensional N-doped super-hydrophilic carbon electrodes with porosity tailored by Cu_2O template-assisted electrochemical oxidation to improve the performance of electrical double-layer capacitors. *Journal of Materials Chemistry A: Materials for Energy and Sustainability*, 2021, 9(5): 2928–2936
 38. Bose N, Sundararajan V, Prasankumar T, Jose S P. $\alpha\text{-MnO}_2$ coated anion intercalated carbon nanowires: a high rate capability electrode material for supercapacitors. *Materials Letters*, 2020, 278: 128457–128468
 39. Mothkuri S, Gupta H, Jain P K, Rao T N, Padmanabham G, Chakrabarti S. Functionalized carbon nanotube and MnO_2 nanoflower hybrid as an electrode material for supercapacitor application. *Micromachines*, 2021, 12(2): 213–228
 40. Zhang J, Zhu T, Wang Y, Cui J, Sun J, Yan J, Qin Y, Zhang Y, Wu J, Tiwary C S, Ajayan P M, Wu Y. 3D carbon coated NiCo_2S_4 nanowires doped with nitrogen for electrochemical energy storage and conversion. *Journal of Colloid and Interface Science*, 2019, 556: 449–457

41. Guo X, Bai N, Tian Y, Gai L. Free-standing reduced graphene oxide/polypyrrole films with enhanced electrochemical performance for flexible supercapacitors. *Journal of Power Sources*, 2018, 408: 51–57
42. Kim D K, Kim N D, Park S K, Seong K D, Hwang M, You N H, Piao Y. Nitrogen doped carbon derived from polyimide/multiwall carbon nanotube composites for high performance flexible all-solid-state supercapacitors. *Journal of Power Sources*, 2018, 380: 55–63
43. Qin T, Dang S, Hao J, Wang Z, Li H, Wen Y, Lu S, He D, Cao G, Peng S. Carbon fabric supported 3D cobalt oxides/hydroxide nanosheet network as cathode for flexible all-solid-state asymmetric supercapacitor. *Dalton Transactions*, 2018, 47(33): 11503–11511
44. Zhang Z, Xiao F, Xiao J, Wang S. Functionalized carbonaceous fibers for high performance flexible all-solid-state asymmetric supercapacitors. *Journal of Materials Chemistry A: Materials for Energy and Sustainability*, 2015, 3(22): 11817–11823